Modeling of structural integrity of aged low alloy steels using non-local mechanics

MAGNUS BOÅSEN

Akademisk avhandling som med tillstånd av Kungliga Tekniska Högskolan i Stockholm framläggs till offentlig granskning för avläggande av teknologie doktorsexamen fredagen den 18 september 2020 kl. 10.00 i Ångdomen, Osquars backe 31, Stockholm.

Academic Dissertation which, with due permission of the KTH Royal Institute of Technology, is submitted for public defence for the Degree of Doctor of Philosophy on Friday the 18th of September at 10:00 in Ångdomen, Osquars backe 31, Stockholm.

Doctoral Thesis in Solid Mechanics
KTH Royal Institute of Technology
Stockholm, Sweden 2020

ISBN 978-91-7873-603-4
TRITA-SCI-FOU 2020:024

Printed by: Universitetsservice US-AB, Sweden 2020

Till mina eviga förebilder
Vanja och Curt Boåsen,
Lena Lindström,
mor och far
samt ljuset i mitt liv
Sofia Boåsen

Abstract

Ageing of low alloy steels affects the structural integrity assessment as it most commonly causes embrittlement and a hardening of the material. This is due to the evolution of the microstructure during operation in the specific application. In nuclear applications, the most common causes of ageing of low alloy steels are irradiation and thermal ageing. Embrittlement in this type of materials is generally divided into hardening and non-hardening embrittlement. The formation of clusters or precipitates of solute atoms typically cause the former, and the weakening of grain boundaries generally cause the latter. This thesis is devoted to the development of models that can be used to describe the material properties of aged low alloy steels in terms of plastic properties and fracture toughness, and to the study of the effects of thermal ageing on the mechanical properties of a low alloy steel.

In *Paper I*, a strain gradient plasticity framework is applied in order to capture length scale effects. The constitutive length scale is assumed to be related to the dislocation mean free path and the changes it undergoes during plastic deformation. Several evolution laws for the length scale were developed and implemented in a FEM-code. This was used to solve a test problem in order to probe the effects of the length scale evolution. All length scale evolution laws considered in this study results in a decreasing length scale, which causes an overall softening in cases where the strain gradient dominates the solution. The results are in tentative agreement with phenomena of strain localization that occurs in highly irradiated materials.

In *Paper II*, a scalar stress measure for cleavage fracture is developed and generalized, here called the effective normal stress measure. This is used in a non-local weakest link model which is applied to two datasets from literature in order to study the effects of the effective normal stress measure, as well as to experiments considering four-point bending of specimens containing a semi-elliptical surface crack. The model is shown to reproduce the failure probability of all considered datasets, i.e. well capable of transferring toughness information between different geometries.

In *Paper III*, a thermally aged weld from the Ringhals nuclear power plant is studied experimentally and compared to a reference material using fracture toughness testing. The main objective of the study was to investigate the effect of thermal ageing on the cleavage or brittle fracture toughness, with a specific focus on the effect of crack tip constraint. The testing showed that thermal ageing had enabled brittle fracture initiation from grain boundaries, resulting in a bimodal toughness distribution due to multiple mechanisms for brittle fracture initiation.

In *Paper IV*, the non-local weakest link model in *Paper II* is further developed to account for multiple mechanism brittle fracture. The model is developed for brittle fracture initiation from grain boundaries and second phase particles. The grain boundary mechanism is inferred from simulations of polycrystalline aggregates using crystal plasticity. When applied to the experimental results of *Paper III*, the model is able to describe the fracture toughness distribution with a remarkable accuracy.

Sammanfattning

Åldring av låglegerade stål påverkar utvärderingen av en komponents strukturella integritet eftersom det vanligtvis ger en påföljande förspródning och härdning av materialet. Detta är på grund av hur materialets mikrostruktur utvecklas under drift i specifika användningsområden. Inom kärnteknisk användning är den vanligaste orsaken till åldring av låglegerade stål antingen bestrålning eller termisk åldring. Förspródning i denna typ av material delas vanligtvis upp i härdande och icke-härdande förspródning. Bildandet av kluster eller utskiljningar av legeringsämnen orsakar typiskt den förstnämnda typen, medans den andra orsakas generellt av försvagade korngränser. Den här avhandlingen ägnas till utvecklingen av modeller som kan användas för att beskriva de mekaniska egenskaperna hos åldrade låglegerade stål i termer av de plastiska egenskaperna och brottseghet, samt undersökningar av termisk åldring av låglegerade stål.

I *Artikel I*, används en plasticitetsteori baserad på både den plastiska töjningen samt dess gradient för att kunna fånga längdskalebeteenden. Längdskalan i teorin antas vara relaterad till dislokationernas medelfria väg och förändringen den genomgår vid plastisk deformation. Flera utvecklingslagar för längdskalan har analyserats och implementerats i en finita element kod. Denna implementering har använts för att lösa ett testproblem med syfte att undersöka effekterna av utvecklingen hos längdskalan. Alla utvecklingslagar som presenteras i artikeln ger en minskande längdskala. Fenomenet leder till ett övergripande mjuknande vid fall där den plastiska töjningsgradienten har stor inverkan på lösningen. Resultaten är i preliminär överenstämmelse med de typer av lokalisering av plastisk töjning som observerats i starkt bestrålade material.

I *Artikel II* utvecklas ett generaliserat spänningsmått i syfte att beskriva klyvbrott, här benämnt effektivt normalspänningsmått. Detta har använts i samband med en icke-lokal svagaste länk modell, som har applicerats på två experimentella studier från den öppna litteraturen i syfte att studera effekterna av det effektiva normalspänningsmåttet. Utöver detta presenteras även nya experiment på ytspruckna provstavar under fyrpunktsböj. I artikeln visas att modellen återskapar sannolikheten för brott för alla undersökta experimentuppställningar, d.v.s. modellen visas vara väl duglig för att överföra brottseghet mellan geometrier.

I *Artikel III* undersöks ett termiskt åldrat svetsgods från Ringhals kärnkraftverk experimentellt genom brottseghetsprovning och jämförs mot ett referensmaterial. Det huvudsakliga målet med studien har varit att undersöka effekten av termisk åldring på den spröda brottsegheten med ett specifikt fokus på effekten av *crack tip constraint*. Provningen påvisade att den termiska åldringen möjliggjorde initiering av sprödbrott från korngränser, med en påföljande bimodal brottseghetsfördelning på grund av initiering av sprödbrott från flera mekanismer

I *Artikel IV* vidareutvecklas den icke-lokala svagaste länk modell som presenterades i *Artikel II* till att ta hänsyn till flera mekanismer för sprödbrottsinitiering, mer specifikt, initiering från korngränser och sekundärfas partiklar. Mekanismen som beskriver korngränsbrott har tagits fram genom att studera polykristaller med hjälp av kristallplasticitet. När modellen appliceras på de experimentella resultaten från *Artikel III* lyckas den återge brottseghetsfördelningen särdeles väl.

Acknowledgements

The work presented in this thesis has been carried out at Solid Mechanics, KTH Royal Institute of Technology, Stockholm between April 2016 and May 2020. The work has been funded by the Swedish Radiation Safety Authority SSM, the Swedish Centre for Nuclear Technology SKC, and Nordic nuclear safety research NKS. All sources of funding are gratefully acknowledged.

It is hard to accurately define what makes a good teacher, but somehow you will always know when you have had one. I know that I have had several during my studies at KTH, without them I would not be who I am today. Three specific teachers that I would like to acknowledge are my supervisors. My main supervisor Pål Efsing has a great mind and a big heart – together we shaped this project into what is presented in this thesis and through this became good friends – and for his support I am grateful. My co-supervisors Carl Dahlberg and Jonas Faleskog served as mentors within their respective and shared fields, for their support I am grateful.

Over the course of my time at the department, I met colleagues and students who have made a lasting impression on me. I would like to acknowledge my office mate, Carl-Magnus Everitt, for providing friendly support and enduring my ramblings. I would also like to mention my good friend Armin Halilović whom I met during my first day at the Department of Solid Mechanics, since then we have been good friends, for which I am grateful.

Collaboration with the very competent Kristina Lindgren has been a great opportunity, which has developed my skills and way of thinking of the micro- and nanostructure of materials.

This project has received a great deal of attention and support within the materials groups of the nuclear power plants in Sweden. This has afforded me opportunities otherwise unattainable in an academic environment. Specifically, I would like to acknowledge Ringhals AB for supplying material and being a constant sounding board for ideas. Greatly acknowledged is Jenny Roudén for always answering my questions, calls, and reading my paper drafts. Also acknowledged at Ringhals are: Björn Forsgren, Johan Blomström, Kerstin Richnau, Per Waernqvist, Fredrik Andreasson, and Per Nilsson. For their support I am grateful.

The experimental effort in Paper III of this thesis would not have been made possible without the continuous support of Martin Öberg. His availability is greatly acknowledged and I am grateful for his mentorship and forbearance. Also, when conducting experiments there is a constant need for workshop manufacturing or adjustments. For this, I would like to acknowledge Göran Rådberg and Jörgen Jansson for their helpfulness and availability.

Furthermore, I would like to acknowledge Ulla Ehrnstén and Marketta Mattila for the micro- and macrographs of the welds presented within the thesis.

Stockholm, May 2020
Magnus Boåsen

List of appended papers

Paper I: *Evolution of the length scale in strain gradient plasticity*

Carl F.O. Dahlberg and Magnus Boåsen
International Journal of Plasticity, vol. 112, 2019, p.220-241

Paper II: *A generalized probabilistic model for cleavage fracture with a length scale - Influence of stress state and application to surface cracked experiments*

Magnus Boåsen, Mateusz Stec, Pål Efsing, Jonas Faleskog
Engineering Fracture Mechanics, *vol*. 214, 2019, *p*.590-608

Paper III: *Analysis of thermal embrittlement of a low alloy steel weldment using fracture toughness and microstructural investigations*

Magnus Boåsen, Kristina Lindgren, Martin Öberg, Mattias Thuvander, Jonas Faleskog, Pål Efsing

TRITA-SCI-RAP 2020:004. *Solid Mechanics, KTH Royal Institute of Technology, Stockholm, Sweden.*

Paper IV: *A weakest link model for multiple mechanism brittle fracture – Model development and application*

Magnus Boåsen, Carl F.O. Dahlberg, Pål Efsing, Jonas Faleskog

TRITA-SCI-RAP 2020:005. *Solid Mechanics, KTH Royal Institute of Technology, Stockholm, Sweden.*

In addition to the appended papers, the work has resulted in the following publications:

On flux effects in a low alloy steel from a Swedish reactor pressure vessel
Magnus Boåsen, Pål Efsing, Ulla Ehrnstén
Journal of Nuclear Materials, vol. 484, 2017, p.110-119

Evolution of precipitation in reactor pressure steel welds under neutron irradiation
Kristina Lindgren, Magnus Boåsen, Krystyna Stiller, Pål Efsing, Mattias Thuvander
Journal of Nuclear Materials, vol. 488, 2017, p.222-230

Cluster formation in in-service thermally aged pressurizer welds
Kristina Lindgren, Magnus Boåsen, Krystyna Stiller, Pål Efsing, Mattias Thuvander
Journal of Nuclear Materials, vol. 504, 2018, p.23-28

Thermal ageing of low alloy steel weldments from a Swedish nuclear power plant – a study of mechanical properties
Magnus Boåsen, Kristina Lindgren, Jenny Rouden, Martin Öberg, Jonas Faleskog, Mattias Thuvander, Pål Efsing
Fontevraud 9, conference proceedings and presentation, 2018, Avignon, France

Thermal ageing of low alloy steel weldments from a Swedish nuclear power plant – the evolution of the microstructure
Kristina Lindgren, Magnus Boåsen, Krystyna Stiller, Pål Efsing, Mattias Thuvander
Fontevraud 9, conference proceedings, 2018, Avignon, France

Contribution to the papers

The author’s contributions to the appended papers are as follows:

Paper I:
Boåsen derived and proposed assumptions for several of the evolution laws presented in the paper. All the numerical implementation and about half of all the simulations were carried out by Boåsen. In the writing process, Boåsen was active in finding relevant references and wrote about half of the paper.

Paper II:
Boåsen wrote the program code used for all the post-processing described in the paper. The effective normal stress measure was derived by Boåsen. All the used finite element models were created and run by Boåsen. In the writing process, Boåsen wrote most of the paper.

Paper III:
Boåsen planned the experiments and the manufacturing, as well as executing the experiments and the analysis. The manuscript was written mostly by Boåsen. Dr. Lindgren carried out the nanostructural investigations and analysis.

Paper IV:
Boåsen identified the necessary modeling framework needed and derived the multiple mechanism weakest link model. Boåsen came up with the idea to utilize crystal plastic modeling to infer the g_1-function and subsequently the analytical model. Boåsen implemented the porous plastic Gurson model together with Faleskog. Boåsen carried out all modeling and analysis. Boåsen wrote the paper.

Contents

1. Introduction 1

 1.1. Aims of this study 2

 1.2. Structure 2

2. On the ageing effects on the mechanical properties of low alloy steels 3

 2.1. Low alloy steel and associated weld metal 3

 2.2. Ageing of low alloy steels 6

3. Modeling concepts of ageing effects 11

 3.1. Hardening and changes of plastic properties 11

 3.2. Single mechanism weakest link modeling of cleavage fracture 17

4. Fracture toughness of a thermally aged low alloy steel weld.........................23

5. Multiple mechanism weakest link modeling of brittle fracture......................29

6. Future work 35

Bibliography 37

Summary of appended papers...42

Paper I

Paper II

Paper III

Paper IV

1. Introduction

The importance of electrical power to the development of society cannot be overstated. Production of electricity comes in many forms and is largely dependent on natural resources such as oil, coal, rivers, biomass and fissile material, and to a minor extent on sun and wind. The dependence on fossil fuels (oil, coal) for production of electricity results in the release of large quantities of CO_2. A greenhouse gas, CO_2 contributes to climate change through the greenhouse effect as well as other types of altered environmental conditions, such as those brought forth by e.g. ocean acidification. Nuclear power can be used as a stable source of electricity production (as opposed to intermittent sources such as wind and solar) with very little CO_2 generated per TWh of electricity produced compared to other sources. As electrical power increases the standard of living in societies around the world, it could be of interest to understand the impact from different energy sources on life itself. One study estimates the mortality in terms of loss of human life per TWh of produced electricity for nuclear power to be 0.01, which in the same study is compared to solar which has a doubled mortality rate and wind with a tripled mortality rate in relation to nuclear [1]. Another study compares nuclear to fossil-based power generation, where the mortality rate of coal power in Europe is 387 times higher than that of nuclear [2].

Sweden obtains a large share (40 % [3]) of its electricity from nuclear power. Some of the Swedish reactors are coming close to the end of their originally designed life-times and will face decommissioning, and some of the reactors are undergoing life extension programs. It is therefore especially important to understand the effects of long-term operation on the materials used in the reactors. For instance, the reactor pressure vessel is made from welded plates and/or forgings of low alloy steel. Low alloy steels are alloys containing primarily iron (Fe) and low amounts of alloying elements (1.5-5 %), typically Mn, Si, Ni, Mo, Cr and V. The reactor pressure vessel is subjected to neutron irradiation originating from the core, and an operating temperature of ~290 ˚C. This environment causes the low alloy steel and its weldments to become embrittled due to ageing, which reduces the size of the operating window in terms of pressure and temperature, as well as the operating limits and design transients. Therefore, regular safety assessments at timed intervals are conducted in order to ensure maintained operability of the reactor. It is also important to realize that replacement of a reactor pressure vessel is very complicated and very costly.

1.1. Aims of this study

This thesis is the culmination of a PhD-project with the aim of studying the effects of ageing on the mechanical properties of low alloy steels in nuclear reactors. The work has included study and development of modeling concepts and frameworks for modeling the ageing effects on low alloy steels, and an experimental investigation of thermal ageing of a pressurizer from a pressurized water reactor. The thesis contains four papers, with the first two presenting two possible modeling pathways for studying ageing induced effects on the relevant mechanical properties of low alloy steels. The latter two are concerned with an experimental program and the modeling of fracture toughness tests of aged low alloy steel weldments.

1.2. Structure

The thesis is outlined as follows; Section 2 presents a general review of the most pertinent effects of ageing with respect to micro- and nanostructure as well as key effects related to mechanical properties and embrittlement. Its purpose is to put the appended papers in the correct context. Section 3 contains a short review of the key aspects related to the first two appended papers as well as an excerpt of key results. Section 4 is concerned with the content of Paper III, where an experimental series of a thermally aged material is tested and compared to the results of a reference material from the same test series. Section 5 is relevant to Paper IV, where a modeling framework for multiple mechanism brittle fracture is presented and applied to the test results of Paper III. Section 6 presents some possible considerations for future work.

2. On the ageing effects on the mechanical properties of low alloy steels

2.1. Low alloy steel and associated weld metal

Reactor pressure vessels are commonly made from low alloy steels which have a ferritic or ferritic/bainitic microstructure and are chosen due to their good mechanical properties, e.g. fracture toughness. However, the fracture toughness of these steels exhibits a strong temperature dependence. At low temperatures, ferritic steels are brittle and have a failure mode commonly called cleavage fracture. This type of fracture is typically initiated due to slip induced cracking of a second phase particle, which nucleates a micro crack that starts propagating dynamically [4], [5]. In order for such a micro crack to develop into a critical cleavage crack, it must propagate across microstructural obstacles such as high angle grain boundaries [6], [7], [8]. For this to happen, the micro crack needs to have been nucleated in a region where the stress is high enough over a sufficiently large distance [9], [10]. If all obstacles in the vicinity of the initial crack nucleus can be overcome, the crack develops into a macroscopic cleavage crack which results in a drastic failure. At increasing temperature, the material becomes more ductile, until eventually the cleavage failure mode is suppressed. This suppression is accompanied by a shift to a ductile failure mode, which becomes dominant. This transition is called the ductile-to-brittle transition and is commonly defined by the temperature at which the transition is occurring. This temperature is typically determined from one of two methods, the older method being impact testing, where the temperature at 41 J of absorbed energy, T_{41J}, is used to define the transition. The more recent method relies on fracture toughness testing according to the master curve methodology to determine the reference temperature T_0, which is the temperature at which the median fracture toughness is 100 $\mathrm{MPa}\sqrt{\mathrm{m}}$ [11]. The typical result of both methods is used to illustrate the ductile-to-brittle transition in Figure 1.

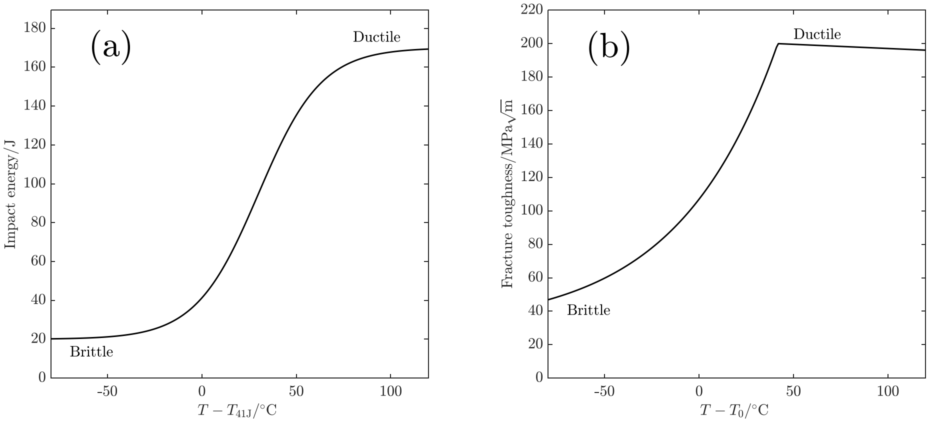

Figure 1. Illustration of the ductile-to-brittle transition for a typical low alloy steel as measured by (a) Charpy impact testing, and (b) fracture mechanical testing through the master curve methodology.

The multi-layer weld metal of reactor pressure vessels made from low alloy steel will obtain a ferritic or ferritic/bainitic microstructure similarly to the plates and forgings and therefore also exhibits the same type of temperature dependent fracture modes. Typically, a weld in a reactor pressure vessel consists of roughly 280 layers; each layer is called a weld bead, which gives rise to a complex microstructure. This complexity lies in the grain structure, which is different compared to that of the plates or forgings due to the nature of welding. As a weld bead solidifies, a dendritic grain structure emerges transverse to the welding direction. As the multi-layer weld is built up, subsequent weld beads will be laid on top of the already existing beads, thus effectively heat treating the upper part of the weld bead below. This gives rise to a region with smaller equiaxed grains in the bead below due to recrystallization from the locally increased temperature. As this process continues, the weld will achieve a microstructure that has regions of dendritic grains, regions with finer grains that have been reheated once and regions that have been reheated several times. These variations in the microstructure can be clearly seen in the macrograph in Figure 2. The micrograph in Figure 3 shows a detailed image of region 2 in Figure 2, illustrating the reheated region between two weld beads containing an equiaxed grain structure. This varying microstructure of welds gives rise to mechanical properties that vary dependent on position.

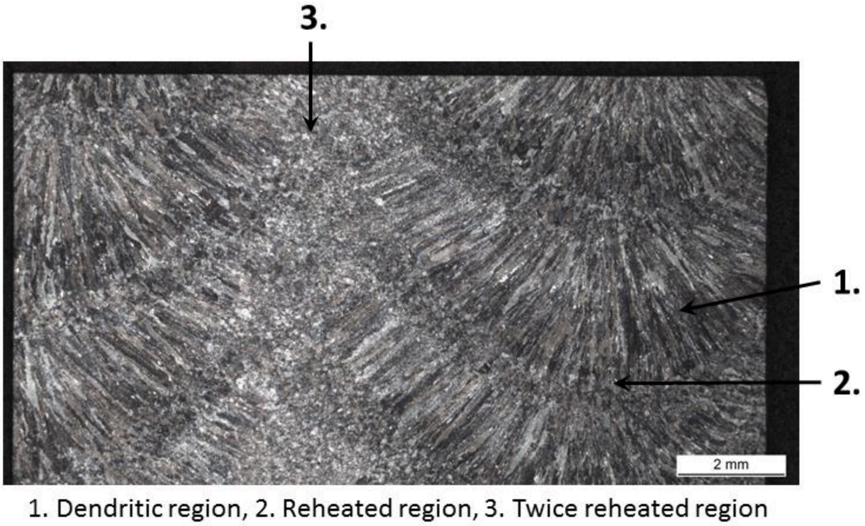
3.
1.
2.
2 mm
1. Dendritic region, 2. Reheated region, 3. Twice reheated region

Figure 2. Weld macrograph displaying the grain microstructure characteristic to multi-layer welds. Image courtesy of Ulla Ehrnstén.

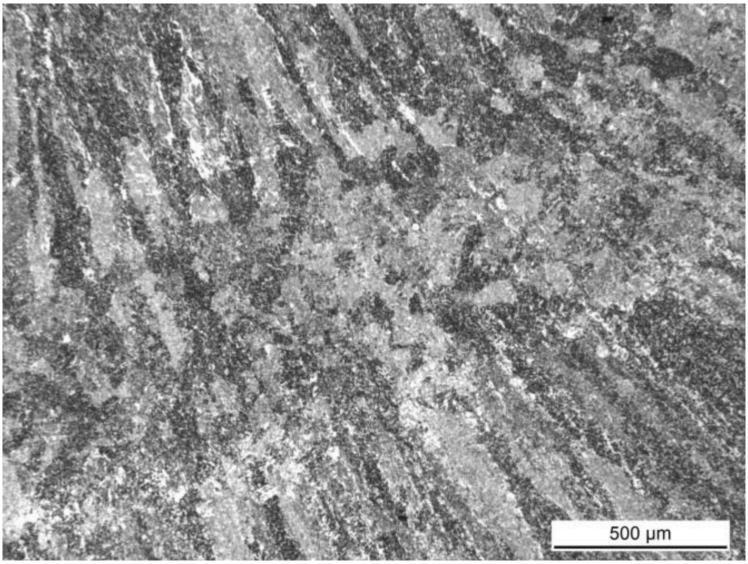

Figure 3. Micrograph displaying the region containing equiaxed grains between regions of dendritic grains. Image courtesy of Ulla Ehrnstén.

2.2. Ageing of low alloy steels

The ageing of low alloys steels due to neutron irradiation and thermal ageing is seen in changes of the mechanical properties due to alterations in the micro- and nanostructure of the metal. Ageing is commonly referred to as embrittlement due to a decrease in toughness of the material. The word ageing will be used alongside with and encompasses embrittlement throughout this thesis.

In general terms it can be said that ageing affects the plastic properties and causes an embrittlement of the material. This emerges as an increase in yield strength, a decreased work hardening slope and a shift in the transition temperature from lower to higher. Changes in the plastic properties of the material are due to the formation of microstructural features such as solute clusters (which may become precipitates) and in the case of irradiation, also matrix damage. In the case of irradiation ageing of the Swedish reactors Ringhals units 3 and 4 (R3 and R4), the shift in mechanical properties was larger than expected. There was also no evidence of any embrittlement saturation, which has been suggested from observations in other cases of irradiated steels where Cu was the main embrittling solute. The alloying content of the weld metal in R3 and R4 is high in Mn and Ni (~1.5 %) and rather low in Cu (0.05 %) and P (0.015 %). Under irradiation, this gives rise to the formation of evenly distributed solute clusters containing primarily Mn, Ni and low amounts of Cu [12], [13], [14]. Matrix damage can emerge under irradiation in the form of vacancy or interstitial clusters, i.e. nano sized voids and dislocation loop-like structures [15], [16]. These types of features all act to increase the resistance to dislocation motion, thus changing the plastic properties of the material.

Investigations of the weld metal (submerged arc weld) of the replaced pressurizer in the Ringhals unit 4 reactor system indicated a large degree of embrittlement and hardening relative to what was expected. The weld metal in this component has similar alloying content to the welds of the reactor pressure vessel, but the operating temperature is at 345 ˚C (cf. ~290 ˚C) and it is not subjected to neutron irradiation. Solute clusters were found using atom probe tomography situated primarily on dislocations and grain boundaries [17]. The difference between thermally aged and neutron irradiated steels can be explained by how solutes segregate and form clusters during irradiation versus in purely thermal conditions. Solute atoms such as the ones found in the clusters are dragged by interstitials and vacancies towards sinks where solute clusters will form, i.e. dislocations, grain boundaries and radiation induced defects such as nano sized voids or dislocation loops [18], [19]. During irradiation, there exists a flux of both interstitials and vacancies due to the interaction between neutrons and the lattice. In the absence of irradiation, i.e. pure thermal conditions, the number of vacancies outnumber the interstitials due to a lower thermal activation energy barrier of vacancies. Thus, at thermal conditions, the alloying elements will be dragged by vacancies to existing sinks such as dislocations and grain boundaries, which offers an explanation to why solute clusters have been observed there in the thermally aged welds from the Ringhals pressurizer. In contrast, evenly distributed clusters were found in the irradiated R3 and R4 welds, where evenly distributed sinks appear due to the interaction between the neutrons and the lattice. The difference in the nanostructure between irradiated weld metal from the Ringhals 4 reactor pressure vessel and the thermally aged pressurizer is illustrated in Figure 4, where more clusters are evident in the irradiated material due to the radiation induced defects.

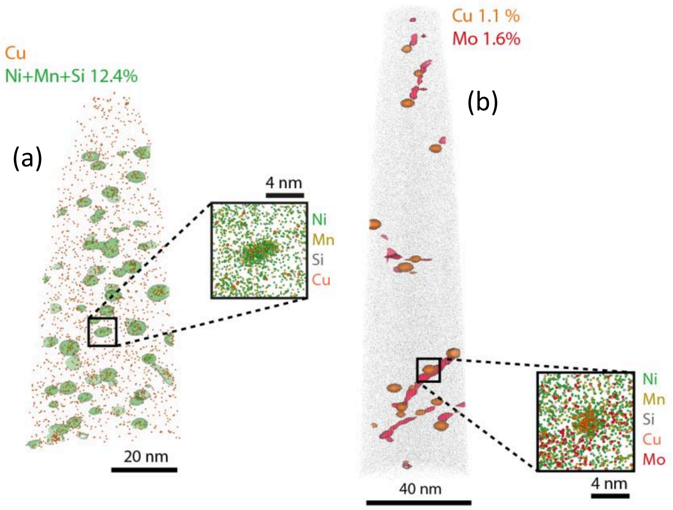

Figure 4. Atom Probe Tomography reconstruction of the nanostructure of (a) irradiated weld metal, and (b) thermally aged weld metal. Image courtesy of Dr. Kristina Lindgren.

As briefly mentioned above, plastic properties are altered due to the formation of the solute clusters. The effects of irradiation on the plastic properties of structural nuclear materials have been observed to cause an increase in yield strength along with a decreased work hardening and in cases of very high irradiation dose, a yield point drop (drop in stress level post initial yielding). For instance, in a study by Farell et al. [20] tensile testing of highly irradiated BCC (low alloy steel), FCC and HCP materials revealed a significantly increased yield stress coupled with a drop in stress right after the yield point and a reduced ductility in the studied materials. This phenomenon has been observed in several material systems and states. For example, in a study by Cotrell and Stokes [21], aluminum (FCC) was studied where a sharp yield point drop was observed after pre-straining at a low temperature with resumed straining at a higher temperature. Luft [22] noted similar phenomena of yield point drop along with work softening when studying precipitation hardened molybdenum and quenched or neutron irradiated metals (both BCC and FCC). The mechanism behind the yield point drop in aged reactor structural alloys is linked to dislocation channel deformation, where plastic deformation concentrates in distinct bands in the microstructure [20], [22]. Inside these bands, also called *clear bands*, the irradiation induced obstacles to dislocation motion have been cleared away by previous dislocation motion. Thus, the resistance to dislocation motion is significantly lower compared to the surrounding material, and therefore plastic deformation tends to localize there.

Embrittlement of low alloy steels appears as a lowered toughness and an increased ductile-to-brittle transition temperature due to ageing. Embrittlement is commonly divided into two categories, hardening and non-hardening embrittlement. The former is due to an increase in yield strength that gives higher stresses ahead of a crack front, *ceteris paribus,* and thus higher probability of a micro crack reaching a critical state for brittle cleavage fracture. This example of how hardening affects embrittlement is somewhat simplified, since other factors affecting the cleavage properties could change at the same time due to ageing. In a publication by Sokolov et al. [23] irradiation embrittlement of a reactor pressure vessel weld metal was studied through the use of fracture, impact and tensile testing. The study revealed a shift of ΔT_0 = 165 ˚C accompanied with an increase in room temperature yield strength of $\Delta\sigma_y = 226$ MPa. In the paper it was also shown how the ductile *J-R* curve was lowered due to irradiation. The latter, non-hardening embrittlement, works by increasing the probability of failure by brittle fracture without the formation of features which impede dislocation motion (not causing hardening). This type of embrittlement is caused by the introduction of a second source of micro crack nucleation sites: grain boundaries weakened due to segregation of impurity elements, increasing the probability for brittle intergranular failure. In the extensive review of intergranular failure in steels by Briant and Banerji [24], it is noted that some distinguishable phenomena appear to be related to intergranular failure. One being that segregation of elements from groups IV-VI in the periodic system appears to yield the most potent grain boundary embrittlement, which is also mentioned by McMahon [25]. These groups include elements such as Si, Sn, P and S, which are not uncommon impurities or alloying elements in the steels of interest. As an example, in a study by Shtrombakh et al. [26] thermal ageing after exposure times up to ~200 000 h of several Russian reactor pressure vessel steels were investigated. It was found that ageing only affected the weld metal with a rather high Ni content, and that the embrittlement was mainly due to impurity segregation resulting in intergranular fracture, i.e. non-hardening embrittlement.

3. Modeling concepts of ageing effects

This section presents the proposed framework for modeling ageing induced changes to the mechanical properties of low alloy steels.

3.1. Hardening and changes of plastic properties

As outlined in Section 2.2, significant changes to the plastic properties emerge as a consequence of the ageing of structural nuclear alloys, such as low alloy steels. Since these changes emerge due to the formation of microstructural features that affect the dislocation motion and overall dislocation behavior, strain gradient plasticity (SGP) theory was chosen for building a modeling framework capable of retracing the main characteristics of ageing induced changes of the plastic properties. SGP offers a way of introducing a size dependent plastic constitutive behavior by allowing the plastic strain gradient to carry constitutive information. The SGP formulation considered here was developed by Gudmundson [27] and is a higher order continuum theory where the plastic strain gradient contributes to the work per unit volume along with the plastic and elastic strains. The internal virtual work in a volume can be expressed as

$$\delta w_i = \int_V \left[\sigma_{ij} \delta\varepsilon_{ij}^{\mathrm{e}} + q_{ij} \delta\varepsilon_{ij}^{\mathrm{p}} + m_{ijk} \delta\eta_{ijk}^{\mathrm{p}} \right] dV, \tag{1}$$

where q_{ij} and m_{ijk} are higher order stress tensors, which are work conjugated to the plastic strain $\delta\varepsilon_{ij}^{\mathrm{p}}$ and the plastic strain gradient $\delta\eta_{ijk}^{\mathrm{p}} \equiv \delta\left(\partial\varepsilon_{ij}^{\mathrm{p}} / \partial x_k\right)$, respectively. The corresponding strong form of (1) are two sets of equilibrium equations

$$\begin{aligned} &\frac{\partial \sigma_{ij}}{\partial x_j} = 0, \\ &\frac{\partial m_{ijk}}{\partial x_k} + s_{ij} - q_{ij} = 0, \end{aligned} \tag{2}$$

where s_{ij} denotes the deviatoric part of σ_{ij}.

The Cauchy stress tensor σ_{ij} and the elastic strain $\varepsilon_{ij}^{\mathrm{e}}$ are related through the standard isotropic Hooke's law. Effective scalar measures of stress and plastic strain are defined analogously to J_2-plasticity, which is a formulation for plastic deformation assuming that all plastic deformation is deviatoric in nature, i.e. only undergoes shape change, no volume change. The effective stress Σ and strain rate $\dot{E}^{\mathrm{p}}$ are expressed as

$$\Sigma = \sqrt{\frac{3}{2}\left(q_{ij}q_{ij} + \frac{m_{ijk}m_{ijk}}{l^2} \right)}, \quad \dot{E}^{\mathrm{p}} = \sqrt{\frac{2}{3}\left(\dot{\varepsilon}_{ij}^{\mathrm{p}}\dot{\varepsilon}_{ij}^{\mathrm{p}} + l^2 \dot{\eta}_{ijk}^{\mathrm{p}}\dot{\eta}_{ijk}^{\mathrm{p}} \right)}, \tag{3}$$

where l is the intrinsic constitutive length scale, which will be further addressed below. Following from this formalism, effective scalar measures of the plastic strain increment and strain gradient increment can be expressed as

$$\dot{\varepsilon}^{\mathrm{p}} = \sqrt{\frac{2}{3}\dot{\varepsilon}_{ij}^{\mathrm{p}}\dot{\varepsilon}_{ij}^{\mathrm{p}}}, \quad \dot{\eta}^{\mathrm{p}} = \sqrt{\frac{2}{3}\dot{\eta}_{ijk}^{\mathrm{p}}\dot{\eta}_{ijk}^{\mathrm{p}}}. \tag{4}$$

The current framework would lead to an indeterminacy of the higher order stresses if a rate-independent plastic constitutive model were to be used. Instead, a viscoplastic model is used and the plastic flow rules are expressed as

$$\dot{\varepsilon}_{ij}^{\mathrm{p}} = \dot{\varepsilon}_0 \frac{3q_{ij}}{2\Sigma}\Phi\left(\Sigma, \sigma_{\mathrm{f}}\right), \quad \dot{\eta}_{ijk}^{\mathrm{p}} = \dot{\varepsilon}_0 \frac{3m_{ijk}}{2l^2\Sigma}\Phi\left(\Sigma, \sigma_{\mathrm{f}}\right), \tag{5}$$

where the $\dot{\varepsilon}_0$ is a reference strain rate and σ_{f} is the material flow stress. The viscoplastic potential Φ was chosen to be a Ramberg-Osgood type function as

$$\Phi\left(\Sigma, \sigma_f\right) = \frac{\Sigma}{\sigma_{\mathrm{f}}}\zeta + \left(\frac{\Sigma}{\sigma_{\mathrm{f}}}\right)^n, \tag{6}$$

where the parameter $\zeta > 0$, but $<< 1$, is necessary from a numerical point of view and can be interpreted as the inverse of the initial resistance to plastic flow. The parameter was set to $\zeta = 10^{-9}$, and it only influences the solution (to a small extent) before initial yielding. It should be noted that a rate-independent behavior can be achieved from (6) if the exponent n is chosen to be a sufficiently large number.

The length scale introduced in (3) controls the influence of the plastic strain gradient on the constitutive response. This type of modeling is also called non-local continuum modeling, since the constitutive behavior at a point (local) is informed by its surrounding state (non-local) through the length scale and plastic strain gradient. For instance, if the plastic strain is allowed to vary over a region the size of the length scale or smaller, the response will be significantly affected. If the opposite occurs, the solution starts approaching the classical continuum J_2-plasticity response. As the length scale in this theory is only related to the plastic constitutive behavior, attempts can be made to relate this to the dislocation microstructure of materials of interest. In the study presented in Paper I of this thesis, it is assumed that the length scale l should be related to the dislocation mean free path and the changes it undergoes during plastic deformation. This is done by allowing the length scale to evolve with plastic deformation.

Patterning of the dislocation microstructure is of interest for the modeling of ageing effects on the plastic properties of structural alloys used in nuclear applications. As a starting point for this, Holt's [28] relation for dislocation cell size as a function of dislocation density was used

$$\Lambda = \frac{A}{\sqrt{\rho}}, \tag{7}$$

where Λ is the wavelength representing the average dislocation cell diameter, ρ is the dislocation density, and A is a non-dimensional material parameter. By differentiation of (7), and assuming equivalence between the changes in this microstructural length scale and the constitutive length scale $\mathrm{d}\Lambda = \mathrm{d}l$, a general evolution law for l can be expressed as

$$\mathrm{d}l = -\frac{l^3}{2A^2}\mathrm{d}\rho. \tag{8}$$

As the above outlined theory is an isotropic small strain plasticity framework, it is not possible to reliably compute a dislocation density based on the available fields. However, the effective measures of strain and strain gradient defined in (3) and (4) may serve as isotropic proxies for the dislocation densities with the addition of a few assumptions.

One example of how an evolution law for the length scale was developed is given here; others were also derived and are detailed in Paper I of this thesis. A common assumption about the dislocation density is that the total density is the sum of geometrically necessary dislocations (GND) and statistically stored dislocations (SSD) as $\rho = \rho^{\mathrm{G}} + \rho^{\mathrm{S}}$. However, as noted by Ashby [29], this is an oversimplification that should mainly be valid at small dislocation densities as the presence of ρ^{G} will accelerate the accumulation of ρ^{S}. Nevertheless, incrementally, such an addition of densities should be a valid assumption, i.e. $\mathrm{d}\rho = \mathrm{d}\rho^{\mathrm{G}} + \mathrm{d}\rho^{\mathrm{S}}$. Following arguments by Devincre et al. [30] and Ashby [29], reasonable relations for the GND and SSD densities could be written as

$$\mathrm{d}\rho^{\mathrm{G}} = \frac{1}{b}\mathrm{d}\eta^{\mathrm{p}}, \ \mathrm{d}\rho^{\mathrm{S}} = \frac{1}{bl}\mathrm{d}\varepsilon^{\mathrm{p}}, \tag{9}$$

where dynamic recovery effects on $\mathrm{d}\rho^{\mathrm{S}}$ are neglected, and b is the Burger's vector. By using this in (8) the following evolution law for the constitutive length scale is found

$$\mathrm{d}l = -\frac{l^3}{2A^2b}\left(\mathrm{d}\eta^{\mathrm{p}} + \frac{\mathrm{d}\varepsilon^{\mathrm{p}}}{l}\right) = -Cl^3\left(\mathrm{d}\eta^{\mathrm{p}} + \frac{\mathrm{d}\varepsilon^{\mathrm{p}}}{l}\right), \tag{10}$$

where C is a parameter the physical dimension of 1/length that sets the strength of the length scale evolution.

A consequence of (10) is that the length scale will decrease and asymptotically approach $l = 0$. This indicates that the dislocation density would tend towards infinity, which is physically unreasonable. It could also be noted that if the dislocation density is allowed to increase indefinitely, then the crystalline base structure of the material would become increasingly more amorphous, where one could start to argue about the definition of a dislocation. Due to these reasons, a saturation length scale was introduced, which is related to the maximum dislocation density that can be achieved under plastic deformation. This comes into the evolution law as

$$\mathrm{d}l = -C\left(l - l_{\mathrm{sat}}\right)^{3}\left(\mathrm{d}\eta^{\mathrm{p}} + \frac{\mathrm{d}\varepsilon^{\mathrm{p}}}{l - l_{\mathrm{sat}}}\right), \tag{11}$$

where l_{sat} is the saturation length scale. The main effect of this is that the length scale would asymptotically reach l_{sat} instead of 0, thereby bounding the length scale evolution.

As a test problem to study the effects of the length scale evolution, a pure bending problem was solved using a 2D-plane strain finite element code. This problem was chosen because it gives a well-defined strain gradient through the geometry using only displacement boundary conditions and has a thorough analytical foundation. All boundaries except at the applied displacement are traction free, considering both higher and lower order tractions. The problem was solved using one column of elements and by enforcing pure bending, such that the deformation follows standard small strain Euler-Bernoulli beam theory, i.e. plane cross sections remain plane. For the flow stress of the material, a power law hardening model was used. An illustration of the bending problem and the finite element model along with the displacement boundary conditions used can be seen in Figure 5.

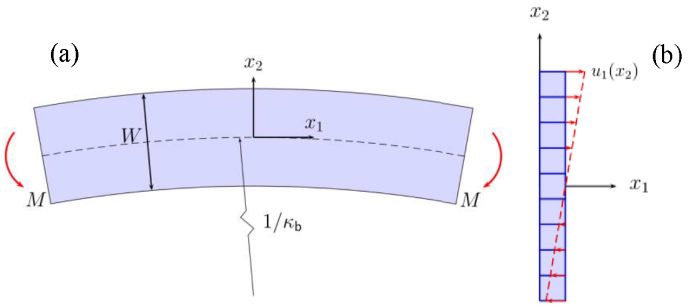

Figure 5. (a) Illustration of the pure bending problem, (b) illustration of finite element discretization and displacement boundary conditions

In Figure 6, the resulting normalized bending moment is shown as a function of the normalized curvature for two different beam thicknesses and different values of the evolution parameter C for the evolution law in (11). The main characteristics of the SGP model are unaffected by the evolving length scale, i.e. a smaller geometrical size produces a stronger response, which presents as a higher yield point. The upper family of curves in Figure 6 represents a beam with $W/l_0 = 3$ where the length scale evolution has distinct effects and the lower family of curves corresponds to a thicker beam with $W/l_0 = 12$ where the effects are less dramatic. Also included is the local theory solution where $W/l_0 \to \infty$ as a dotted line. It can be seen in Figure 6 that the length scale evolution combined with the size effects from the SGP theory results in an increase in the yield strength and a decrease in hardening, and in the more extreme cases also a yield point drop and a significant reduction in the rate of work hardening. This can be explained by the fact that as the length scale reduces, a *loss of non-locality* occurs, which locally, pushes the SGP solution towards the local theory solution. This effect will naturally vary throughout the thickness of the beam due to the variation of the plastic strain and strain gradient. With the formulation in (11) the length scale changes drastically towards the free edge, thus effectively reducing the normal stress at large values of x_2, resulting in a significant reduction of the bending moment due to a reduced length scale.

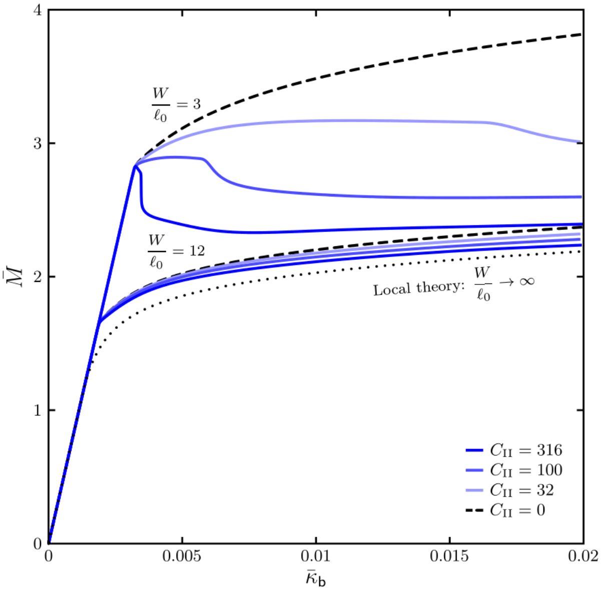

Figure 6. Normalized bending moment versus normalized bending curvature. The two families of curves represent different beam thicknesses. Reference gradient plasticity solutions are presented as dashed lines and the standard J_2-plasticity solution is presented as the dotted line.
The parameter C is normalized by l_0^{-1}, i.e. initial length scale.

These effects on the overall moment-curvature response are in tentative agreement with the general ageing effects that can be seen in low alloy steels and other structural alloys in nuclear applications. However, it is judged that this type of modeling needs far more attention before predictive modeling of effects of actual material ageing on the plastic properties can be carried out for practical purposes.

3.2. Single mechanism weakest link modeling of cleavage fracture

Transferability in fracture mechanics connects the toughness information from laboratory tested specimens to that of an actual defect in a component, such as the reactor pressure vessel. One of the main concerns of this transferability problem is the crack tip constraint, which in part is a geometrical phenomenon, but also an effect of the plastic properties of the material. Crack tip constraint can, in somewhat simplified terms, be explained as the ability to preserve the self-similar stress field ahead of the crack tip. A state of high constraint preserves the high stress state a head of the crack front, resulting in a conservative estimate of the fracture toughness. A state of low constraint will cause a breakdown of the self-similar stress fields through large scale yielding and thus result in higher fracture toughness. Usually, fracture tests are conducted using deeply cracked bend specimens that produce a state of high constraint, while actual defects are typically loaded in tension that generally produces a state of lower constraint. The transferability between the two is not trivial. The cleavage fracture process is strongly dependent on the susceptibility of micro crack nucleation and propagation. As this process is inherently probabilistic in nature, a probabilistic model was chosen as a viable modeling pathway for embrittlement. In Paper II of this thesis, a study is presented, where it is shown that the model of choice is capable of transferring the fracture toughness from high and low constraint laboratory tests to several geometries where loss of constraint occurs. In particular, it is shown that the model can reproduce the failure probability of surface cracked specimens with defects that geometrically resemble those of an actual reactor pressure vessel. In addition to this, we also develop a generalized scalar normal stress measure to be applied in conjunction with the non-local stress tensor. In Paper IV of this thesis, the model will be extended to incorporate the effects of multiple mechanisms of brittle fracture initiation.

The model chosen for modeling failure by brittle cleavage fracture is the model developed by Kroon and Faleskog [10]. This model assumes a weakest link mechanism for cleavage fracture. The basic assumptions of weakest link modeling of cleavage fracture are: (*i*) the total volume, V, of the considered structure can be divided into smaller elements of infinitesimal size where total failure will occur if one of these elements fail. (*ii*) the probability of failure of an element $\mathrm{d}P_\mathrm{f}$, depends on the stress and strain state in the element, and linearly on the volume of the element. Thus $\mathrm{d}P_\mathrm{f} = h(\sigma, \varepsilon)\, \mathrm{d}V/V_0$, where $h(\sigma, \varepsilon)$ is a function describing the random behavior associated with the micro mechanisms of the cleavage event, and V_0 is a reference volume that needs to be chosen together with $h(\sigma, \varepsilon)$. (*iii*) statistical independence of the critical state of the hazard function is assumed between the elements comprising the structure. The model in [10] is based on the assumption that cleavage fracture only occurs due to the simultaneous fulfilment of the statistically independent plastic strain based micro crack nucleation relation and a stress based propagation criterion. The model is outlined as follows, the cumulative probability of failure by cleavage fracture can be expressed as

$$P_\mathrm{f} = 1 - \exp\left(-\int_V h_\mathrm{max} \frac{\mathrm{d}V}{V_0} \right), \tag{12}$$

where h_max is the maximum value of the random function experienced throughout the loading history, V is the volume of the structure, and V_0 is the reference volume. The microstructural process of cleavage fracture comes in as the hazard function $h = h\left(\varepsilon_\mathrm{e}^\mathrm{p}, \bar{\sigma}\right)$, which is chosen as

$$\begin{aligned}
&h\left(\varepsilon_\mathrm{e}^\mathrm{p}, \bar{\sigma}\right) = h_1\left(\varepsilon_\mathrm{e}^\mathrm{p}\right) h_2\left(\bar{\sigma}\right), \\
&h_1\left(\varepsilon_\mathrm{e}^\mathrm{p}\right) = c\varepsilon_\mathrm{e}^\mathrm{p}, \\
&h_2 = \begin{cases} \exp\left(-\left(\dfrac{\eta \sigma_\mathrm{th}}{\bar{\sigma}} \right)^2 \right) - \exp\left(-\eta^2\right), \text{ for } \bar{\sigma} > \sigma_\mathrm{th}, \\ 0, \text{ for } \bar{\sigma} < \sigma_\mathrm{th}. \end{cases}
\end{aligned} \tag{13}$$

In (13), $\varepsilon_\mathrm{e}^\mathrm{p}$ is the effective plastic strain, $\bar{\sigma}$ is a non-local measure of stress, c, σ_th and η are material parameters, where the influence of η has in practical applications been observed to be weak. In Paper II of this thesis, a great deal of time has been devoted to the development of a generalized form of $\bar{\sigma}$.

The scalar non-local stress $\bar{\sigma}$ is attributed significance as it represents the condition that the stress field must be high enough over a sufficiently large volume. The non-local stress is a scalar measure, which is constructed from the non-local stress tensor defined according to the integral

$$\bar{\sigma}_{ij} = \frac{1}{V_\mathrm{L}} \int_{V_\mathrm{L}} \sigma_{ij}\left(\hat{X}_k - X_k\right) \mathrm{d}\hat{V}, \tag{14}$$

where $\mathbf{X}$ are the coordinates at the center of V_L, the volume over which the stress tensor is averaged. From $\bar{\sigma}_{ij}$ the non-local principal stresses $\left(\bar{\sigma}_\mathrm{I}, \bar{\sigma}_\mathrm{II}, \bar{\sigma}_\mathrm{III}\right)$ are calculated. A generalized effective normal stress measure can be constructed from the normal stress acting on a plane. The normal stress on a plane defined by the polar angle φ and the azimuthal angle θ from the principal stress system can be expressed as

$$\bar{\sigma}_\mathrm{n}\left(\varphi, \theta\right) = \bar{\sigma}_\mathrm{I} \cos^2 \varphi + \bar{\sigma}_\mathrm{II} \sin^2 \varphi \cos^2 \theta + \bar{\sigma}_\mathrm{III} \sin^2 \varphi \sin^2 \theta. \tag{15}$$

Integration of (15) combined with a stress distribution function $\rho\left(\varphi, \theta\right)$ over the unit sphere results in an averaged weighted normal stress as

$$\bar{\sigma} = \frac{1}{4\pi} \int_0^{2\pi} \int_0^{\pi} \bar{\sigma}_\mathrm{n}\left(\varphi, \theta\right) \rho\left(\varphi, \theta\right) \sin\varphi \, \mathrm{d}\varphi \, \mathrm{d}\theta. \tag{16}$$

By choosing $\rho\left(\varphi, \theta\right)$ to unity, the integral in (16) evaluates to the mean stress $\bar{\sigma}_\mathrm{m} = \left(\bar{\sigma}_\mathrm{I} + \bar{\sigma}_\mathrm{II} + \bar{\sigma}_\mathrm{III}\right)/3$. However, the stress distribution function $\rho\left(\varphi, \theta\right)$ can be chosen more carefully and should for physical reasons satisfy

$$\frac{1}{4\pi} \int_0^{2\pi} \int_0^{\pi} \rho\left(\varphi, \theta\right) \sin\varphi \mathrm{d}\varphi \mathrm{d}\theta = 1. \tag{17}$$

Choosing $\rho(\varphi, \theta)$ to only depend on the polar angle φ as

$$\rho(\varphi) = (n+1)\cos^n \varphi \quad \text{where } n \geq 0, \tag{18}$$

the integral presented in (16) evaluates to

$$\bar{\sigma} = \frac{(n+1)\bar{\sigma}_{\mathrm{I}} + \bar{\sigma}_{\mathrm{II}} + \bar{\sigma}_{\mathrm{III}}}{n+3}. \tag{19}$$

This is a non-local stress measure that is able to express a state of normal stress over the volume V_{L}, ranging from the mean stress $\bar{\sigma}_{\mathrm{m}}$ when $n = 0$ to the maximum principal stress $\bar{\sigma}_{\mathrm{I}}$ when $n \rightarrow \infty$.

Micro cracks will not always nucleate on a cleavage plane aligned with the axis of the maximum principal stress. Therefore, the measure of effective normal stress in (19) can be interpreted as a phenomenological way of treating the potential triggering of cleavage initiation from a distribution of variously oriented micro cracks and associated cleavage planes. A visualization of the effective normal stress measure can be seen in Figure 7.

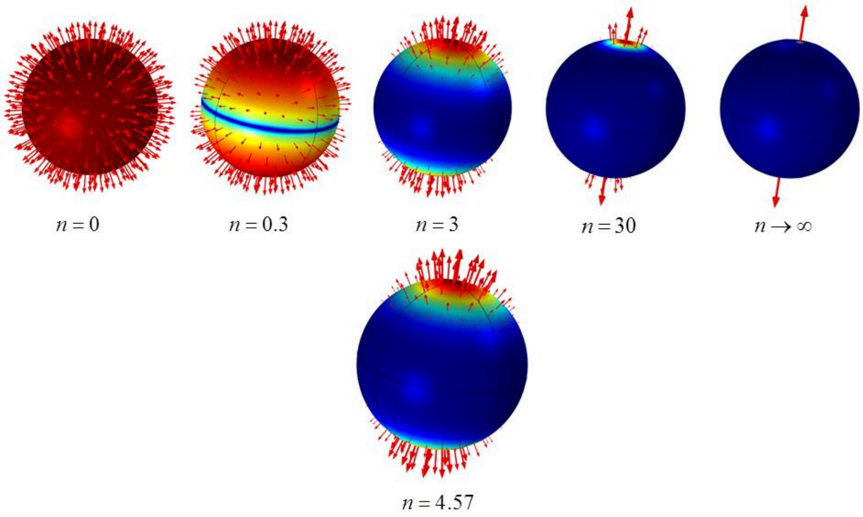

$n = 0$ $n = 0.3$ $n = 3$ $n = 30$ $n \rightarrow \infty$

$n = 4.57$

Figure 7. Visualization of how the effective normal stress changes with the parameter n. Note that the mean stress is obtained when $n = 0$ and the maximum principal stress when $n \rightarrow \infty$.

In Paper II of this thesis, the model outlined above was applied to two data sets pertaining to loss of constraint and is shown to reproduce the effects of constraint on the cleavage fracture toughness of low alloy steels. In Figure 8, an example of calibration and validation of model parameters as well as the influence of the effective normal stress parameter n on the failure probability of SEN(B)-specimens (three-point bend) can be seen.

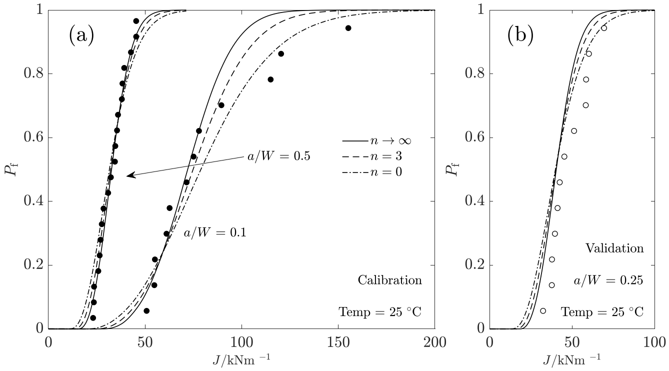

Figure 8. Predicted failure probability of SEN(B) specimens as solid lines tested at room temperature. (a) Subsets where $a/W = \{0.5, 0.1\}$ used for calibration of model parameters, (b) Subset where a/W = 0.25 used for validation of the probabilistic model. Rank probabilities from experiments as circles.

By applying the model to four-point bending experiments of surface cracked specimens containing a semi-elliptical crack, the failure predictions in Figure 9 result. The predictions presented in Figure 9 are all judged to be satisfactory, however, the results for $n=0$ are slightly better than for $n \to \infty$.

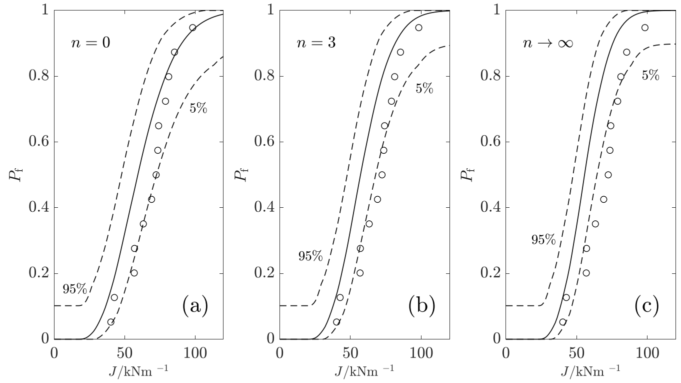

Figure 9. Predicted failure probability of the surface cracked four-point bending experiments as solid lines for different values of the effective normal stress parameter n. Dashed lines represent the 90 % confidence limits for the rank probabilites (a) n = 0, (b) n = 3, and (c) $n \to \infty$. Rank probabilities from experiments as circles.

4. Fracture toughness of a thermally aged low alloy steel weld

The assessment of the structural integrity of any structure made from a ferritic steel requires knowledge of the ductile-to-brittle transition temperature and the related fracture toughness. Typically, this is inferred from laboratory tests, where a conservative high constraint fracture toughness is determined. As stated in Section 3.2, a pertinent issue in the transferability between laboratory tests and the structural integrity of the component is crack tip constraint. With this in mind, research interest was spurred to investigate the effects of ageing on the constraint effect of a low alloy steel.

It was judged that the optimal way to investigate the constraint effect on the fracture toughness would be to include geometries where the crack tip constraint varies, such as three point bend specimens, SEN(B), with different crack to width ratios, e.g. $a/W = \{0.5 \text{ and } 0.1\}$. The deeply cracked specimen creates a state of high constraint, which gives a conservative estimate of the fracture toughness, and the shallowly cracked specimen results in a state of low crack tip constraint. The observation of any differences between two materials in the constraint effect is most effectively carried out by testing a set of high and low constraint specimens at a single temperature per material. The temperature for each material needs to be chosen so that the high constraint fracture toughness of the materials coincides. This experimental procedure makes it straightforward to observe any difference in the sensitivity to crack tip constraint, i.e. any difference in the crack tip constraint effect on the fracture toughness.

Paper III of this thesis presents an investigation where two low alloy steel welds from the Ringhals nuclear power plant in Sweden have been tested according to the outline above. The materials used in the testing included one thermally aged weld from an replaced pressurizer (PRZ) from unit 4 subjected to 345 ˚C for 215 000 h. The other weld from an exchanged reactor pressure vessel head (RPVH) from unit 3 subjected to 310-315 ˚C for 176 000 h was used as a reference, where the effects of thermal ageing were considered to be negligible in comparison to the pressurizer material. The reason that material subjected to operating temperatures had to be used as a reference material was that no archive material was available for the pressurizer welds. The reference material was chosen on account of being very similar in its as-manufactured mechanical properties, such as yield strength and the ductile-to-brittle transition temperature, and also having similar chemical composition to the pressurizer material. The aged material is denoted *R4PRZ* and the reference material is denoted *R3RPVH*.

Testing was conducted by carrying out a pre-series in order to determine the T_0 of each material, from which the test temperatures could be chosen in order to obtain the same high constraint fracture toughness. All tests of high constraint specimens carried out in this investigation, i.e. pre-series and the single temperature tests can be seen in Figure 10, where also the master curve temperature prediction is presented. It is clear that the thermally aged R4PRZ with a T_0 = -33 ˚C is more brittle than R3RPVH with a T_0 = -78 ˚C.

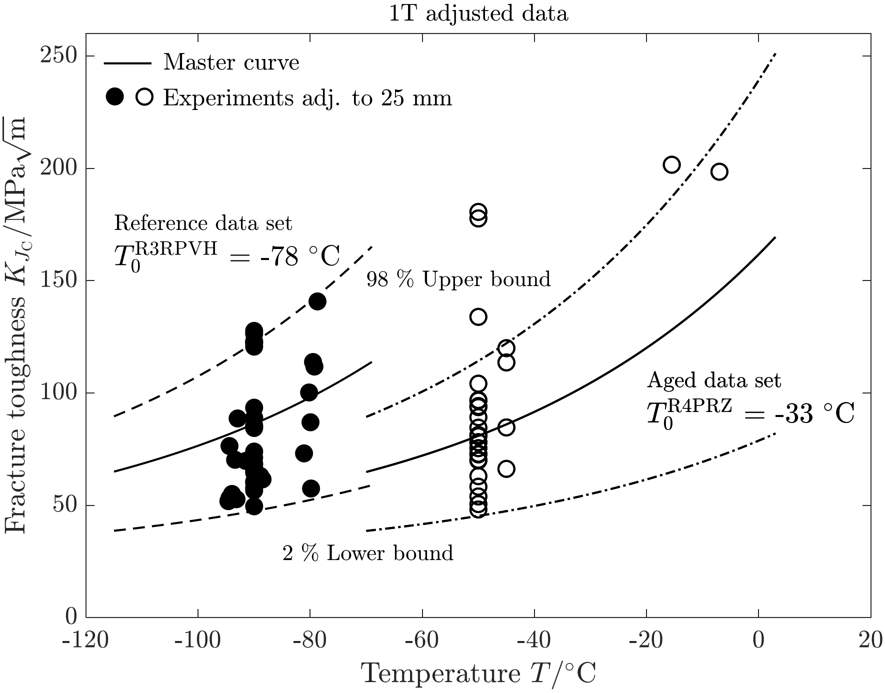

Figure 10. Fracture toughness of individual specimens belonging to both R3RPVH and R4PRZ against testing temperature, and the predicted temperature dependence from the master curve model.

Regarding the results of the single temperature investigation of the constraint effect on fracture toughness, the ranked probability of the R4PRZ tests presents itself as a bimodal toughness distribution as seen in Figure 11, where the effects are most obvious for the shallowly cracked specimens. The specimens containing the shallow cracks present a wide range of fracture toughness. The most brittle specimens display the same toughness as the specimens in the high constraint data set, while in the same data set there are specimens that are subject to significant ductile crack growth before the final brittle failure, displaying a fracture toughness ranging from 9.6 kN/m to 785 kN/m. The results from the reference, R3RPVH, show no traces of any bimodality, being unimodal as would be expected from an as-manufactured ferritic steel, i.e. exhibiting very low to no embrittlement.

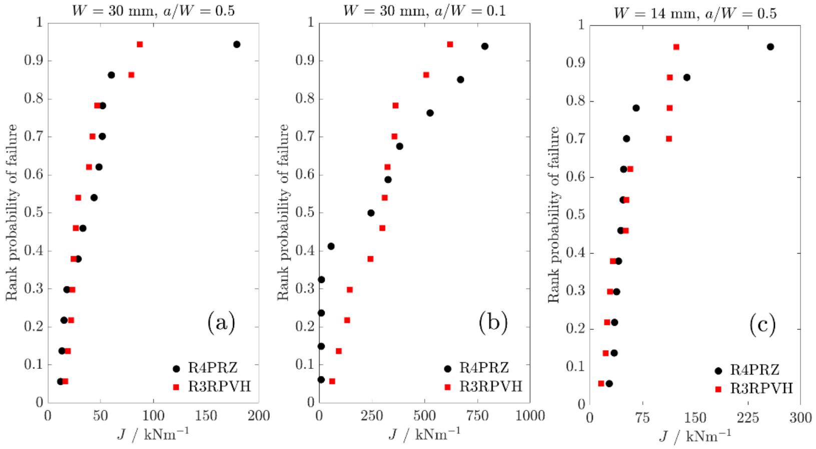

Figure 11. Rank probabilities for the fracture tests of R4PRZ at the test temperature -50 ˚C. (a) Data sets where $W = 30$ mm and $a/W = \{0.5, 0.1\}$. (b) Data set where $W = 14$ mm and $a/W = 0.5$.

Fractographical investigations of the thermally aged R4PRZ unraveled that the low toughness specimens in Figure 11 were subject to brittle fracture initiation stemming from grain boundaries, while the higher toughness specimens displayed a mixture of initiation from second phase particles and grain boundaries. Examples of fractographical images from the investigation can be seen in Figure 12-13. Investigations of the fracture surfaces of R3RPVH were also conducted. It was found that the brittle fracture initiation could be traced back to second phase particles, and that most of the fracture morphology was transgranular with small traces of intergranular fracture in the low toughness specimens.

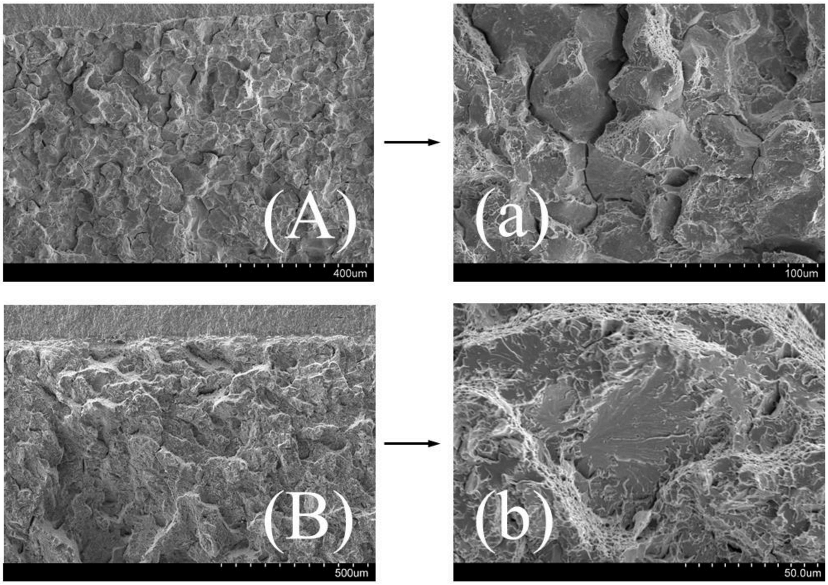

Figure 12. Fractography of deeply cracked specimens ($a/W = 0.5$) from the R4PRZ data set. Specimen {(A), (a)} fractured at a *low* toughness of $K_{JC} = 52\ \mathrm{MPa}\sqrt{\mathrm{m}}$, displays intergranular fracture, note secondary cracks in (a). Specimen {(B), (b)} fractured at a *higher* toughness of $K_{JC} = 108\ \mathrm{MPa}\sqrt{\mathrm{m}}$, displays transgranular fracture, probable initation point in (b).

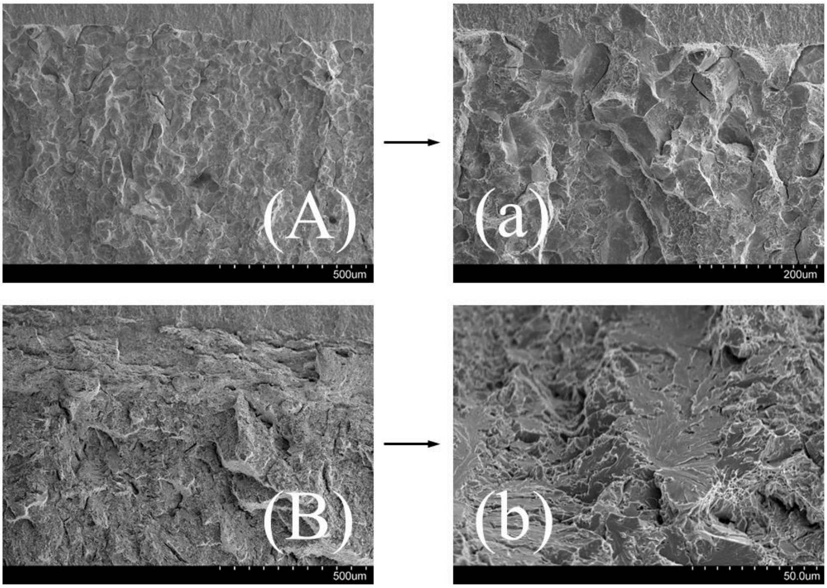

Figure 13. Fractography of shallowly cracked specimens ($a/W = 0.1$) from the R4PRZ data set. Specimen {(A), (a)} fractured at a *low* toughness of $K_{JC} = 50\ \mathrm{MPa}\sqrt{\mathrm{m}}$, displays intergranular fracture, note secondary cracks in (a). Specimen {(B), (b)} fractured at a *higher* toughness of $K_{JC} = 270\ \mathrm{MPa}\sqrt{\mathrm{m}}$, displays transgranular fracture, probable initation point in (b).

Uniaxial tensile testing of the materials investigated in this study indicates that both materials have been subject to hardening during operation. A comparison can be seen in Table 1, where the as-manufactured check-in data is comparted to the results of this study. Hardening due to ageing is commonly ascribed to the formation of solute clusters or fine scale precipitates during operation, which act as obstacles to dislocation motion. Both materials were investigated using APT, where clusters were found present in both materials; however to a far greater extent in the thermally aged R4PRZ than in the reference R3RPVH.

Table 1. Comparison between check-in yield strength and the results obtained in this investigation.

R_{p02}/MPa	Check-in	Current	Difference
R4PRZ	579	656	62
R3RPVH	575	637	77

The thermally aged steel from the Ringhals unit 4 pressurizer appears from this study to have been subjected to both non-hardening as well as hardening embrittlement. This is evidenced by the emergence of a second mode of brittle fracture initiation from grain boundaries besides initiation from second phase particles, resulting in a bimodal fracture toughness distribution. The hardening contribution is obvious in the results of the mechanical properties, which connects to the emergence of solute clusters in the microstructure.

The main finding of this study is that the ageing of low alloy steels may act to suppress the conventional constraint effect on fracture toughness. That is, the additional conservatism that the constraint effect supplies appears to, in part, have disappeared due to the emergence of the intergranular failure mechanism. This effect of ageing has not been observed elsewhere, to the best of the author’s knowledge. Therefore, it is deemed pertinent for the community of structural integrity engineers to further pursue similar investigations of aged low alloy steels.

5. Multiple mechanism weakest link modeling of brittle fracture

The results presented in Section 4 initiated a modeling effort with the purpose of creating a micromechanically informed probabilistic model with multiple failure mechanisms. This was carried out by expanding upon the weakest link framework presented in Section 3.2 and has been documented in Paper IV of this thesis, a short summary of which is given below.

By assuming that brittle failure is governed by a weakest link mechanism and that in each sub volume there are two (or more) different mechanisms that can initiate brittle failure, it follows that the micro crack that develops into a self-sustaining macro crack will stem from either the one or the other mechanism, i.e. it can only have one origin. Mathematically this can be derived by assuming statistical independence or mutual exclusivity. Here, mutual exclusivity has been used and is expressed as as $P(A \cup B) = P(A) + P(B),$ where A and B corresponds to the two mechanisms, which results in an expression for the probability of failure as

$$P_{\mathrm{f}} = 1 - \exp\left(-\left(h^{\mathrm{A}} + h^{\mathrm{b}}\right) \frac{\mathrm{d}V}{V_0} \right), \tag{20}$$

where h^{A} and h^{B} are the hazard functions for the micro mechanisms of failure. More specifically, particle initiated transgranular and grain boundary initiated intergranular failure. In Section 3.2, the corresponding expression to Eq. (20) was calculated by evaluating the maximum value of h throughout the loading history. This methodology was renewed with interpreting the first part, h_1, comprised in the hazard function, $h = h_1(\varepsilon_{\mathrm{p}}) h_2(\bar{\sigma})$, as the number of micro cracks computed by integrating the rate of micro crack nucleation $g_1$as

$$h_1 = \int_0^{\varepsilon_{\mathrm{p}}} g_1\left(\varepsilon_{\mathrm{p}}\right) \mathrm{d}\varepsilon_{\mathrm{p}}. \tag{21}$$

The result of this is that the hazard function will be computed as

$$h^i = \int_0^{\varepsilon_{\mathrm{p}}} g_1^i\left(\varepsilon_{\mathrm{p}}\right) h_2^i\left(\bar{\sigma}\left(\varepsilon_{\mathrm{p}}\right)\right) \mathrm{d}\varepsilon_{\mathrm{p}}, \tag{22}$$

where the function h_2 is carried forward from the framework in Section 3.2 and corresponds to the fraction of the total number of nucleated micro cracks that can be regarded as potential triggering sites for macroscopic brittle fracture. Superscript i denotes the mechanism represented by the hazard function, i.e. grain boundary or particle-controlled failure. In Section 3.2, the model was developed and validated against experiments of brittle fracture tests where initiation occurred from second phase particles. In the formulation of that model, a linear $h_1(\varepsilon_\mathrm{p})$-function was used, which in the framework presented here, corresponds to a g_1-function that is constant. However, no previous experience with how to incorporate grain boundary failure in this framework exists.

With the purpose of making an informed choice of the g_1-function corresponding to the grain boundary mechanism of brittle fracture, crystal plasticity models analogous to the different zones of a weld microstructure were considered. The models used can be seen in Figure 14, where sub figures (a) and (b) are meant to represent the equiaxed regions of a weld microstructure, while (c) and (d) are made to represent the dendritic regions.

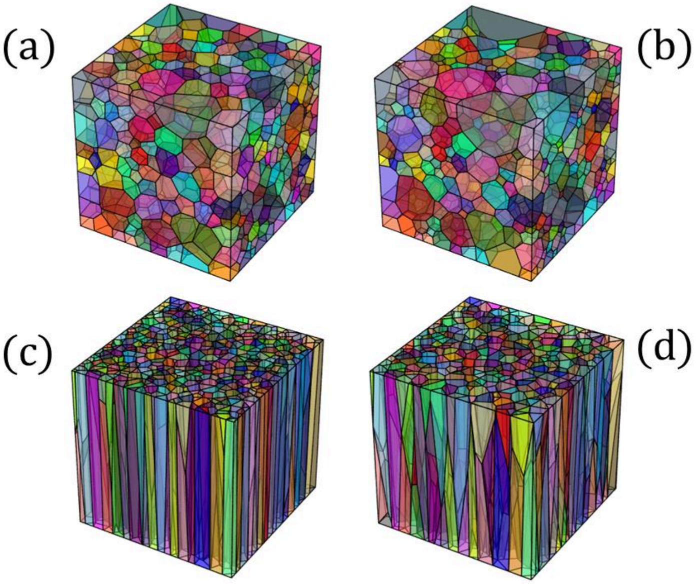

Figure 14. Tesselations of grain structures. (a) and (b) corresponds to the equiaxed grain structures. (c) and (d) correspond to the dendritic grain structures.

The models were solved by supplying boundary conditions through nonlinear kinematic constraints that would yield a constant stress triaxiality $T = (\sigma_{\mathrm{I}} + \sigma_{\mathrm{II}} + \sigma_{\mathrm{III}})/(3\sigma_{\mathrm{e}})$ and Lode parameter $L = (2\sigma_{\mathrm{II}} - \sigma_{\mathrm{I}} - \sigma_{\mathrm{III}})/(\sigma_{\mathrm{I}} - \sigma_{\mathrm{III}})$ through the loading history. In the post-processing of the analysis, the average normal stress acting over each grain boundary has been computed and compared to a critical stress according to a Griffith criterion. If a grain boundary is considered critical, it will be accumulated at that specific time step and not considered for failure in further post-processing.

The models were solved for stress triaxialities in the range $T = \{2.35, 2.2, 2.05, 1.9, 1.75\}$ and for a single Lode parameter value of $L = -0.25$, as the importance of the Lode parameter was early on found to be insignificant. The key result from the crystal analysis can be seen in Figure 15, where the fraction of critical grain boundaries is presented as a function of plastic strain which corresponds to the h_1-function given in (21) and was used to infer the g_1-function. In the analysis of the stress state that emerges in the grain boundaries, it was found that the global stress state is the dominating factor that determines the local grain boundary stress state. This allows for the construction of an analytical model in the same spirit as the crystal model.

In the analytical model of grain boundary failure, the principal stresses are computed from the stress triaxiality and the Lode parameter that together gives the characteristic of the stress state. The effective stress was computed from a flow stress relation, where the plastic strain becomes the loading parameter. This makes it possible to write the stress state as

$$\begin{aligned}
\sigma_{\mathrm{I}} &= \sigma_{\mathrm{e}}\left(T + \frac{3-L}{3\sqrt{L^2+3}}\right),\\
\sigma_{\mathrm{II}} &= \sigma_{\mathrm{e}}\left(T + \frac{2L}{3\sqrt{L^2+3}}\right),\\
\sigma_{\mathrm{III}} &= \sigma_{\mathrm{e}}\left(T - \frac{3+L}{3\sqrt{L^2+3}}\right).
\end{aligned} \tag{23}$$

The number of grain boundaries were set to 5000, the normals were randomly drawn to be uniformly distributed across the unit sphere, and the grain boundary areas were randomly drawn from a log-normal distribution to yield an area distribution akin to the crystal models. In all other regards, the analysis is the same as in the crystal models. Some results from the analytical model are presented and compared to the crystal models in Figure 15, where it can clearly be seen that the analytical model can reproduce the behavior of the crystal model.

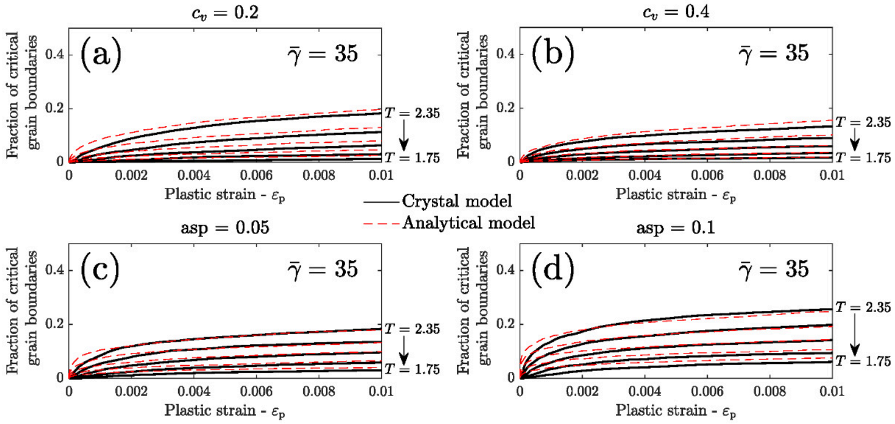

Figure 15. Comparison of the accumulated number fraction of critical grain boundaries between analytical model and the crystal models pertaining to the equiaxed grain structures in (a) and (b), and the dendritic grain structures in (c) and (d). Each line represents a solution where the stress triaxiality T belongs to the set {2.35, 2.2, 2.05, 1.9, 1.75}.

From the results of the crystal and analytical models, two candidates for the g_1-function were constructed as

$$g_1 = \frac{c}{\varepsilon_0\left(1+\dfrac{\varepsilon^{\mathrm{p}}}{\varepsilon_0}\right)}, \tag{24}$$

where ε^{p} is the equivalent plastic strain and

$$g_1 = \begin{cases} \dfrac{c}{\varepsilon_0\left(1+\dfrac{\varepsilon^{\mathrm{p}}}{\varepsilon_0}\right)}\left(T-T_{\mathrm{th}}\right)^2 \quad \text{for} \quad T > T_{\mathrm{th}}, \\ \qquad 0 \quad \text{for} \quad T \le T_{\mathrm{th}}. \end{cases} \tag{25}$$

Here, T is the stress triaxiality and the parameter T_{th} acts as a threshold for the stress triaxiality. The functions presented in Eqs. (24) and (25) could be fitted to the results of the crystal model and the analytical model, respectively, both with a R^2 above 0.99.

Concerning the application of the weakest link model to the fracture toughness tests presented in Section 4 and Paper III of this thesis, i.e. the constraint sensitivity tests of the reference and thermally aged materials. The reference material, which presents a unimodal fracture toughness distribution, is well described by a single mechanism weakest link framework using a constant g_1-function. Predictions of the failure probability of the sets used for parameter estimation and validation can be seen in Figure 16. Clearly, the model is able to predict the fracture toughness distribution with varying constraint and specimen size.

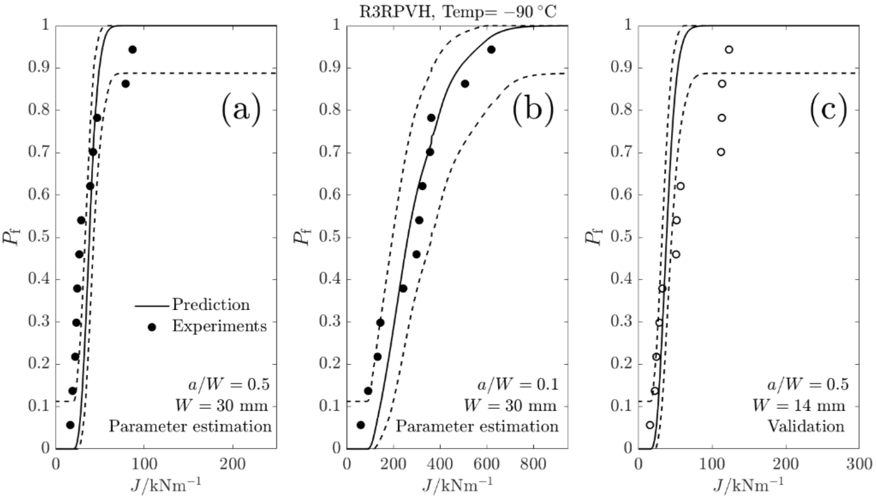

Figure 16. Comparison of the predicted failure probability with rank probabilities for the fracture tests (circles) of the reference material R3RPVH data set tested at a temperature -90 ˚C. (a) subset where $a/W = 0.5$ and $W = 30$ mm, (b) subset where $a/W = 0.1$ and $W = 30$ mm, and (c) subset where $a/W = 0.5$ and $W = 14$ mm. Subsets (a) and (b) were used for parameter estimation, subset (c) were used as validation of model predictions.

The application of the multiple mechanism weakest link model can be seen in Figure 17, where the predictions of the failure probability of the sets used for parameter estimation and validation are presented. Figure 18 shows the same data including an illustration of the underlying brittle fracture mechanisms. The multiple mechanism weakest link model is able to reproduce the fracture toughness distribution with a remarkable accuracy, both in terms of the constraint effect and the size effect. Regarding the choice of g_1 for the brittle fracture mechanism, of the two functions presented in Eqs. (24) and (25), the resulting failure prediction for the data set at hand is more or less the same regardless of which function is used. This may be due to the possibility of the difference in the stress triaxiality being too narrow between the geometries used for parameter investigation and model validation.

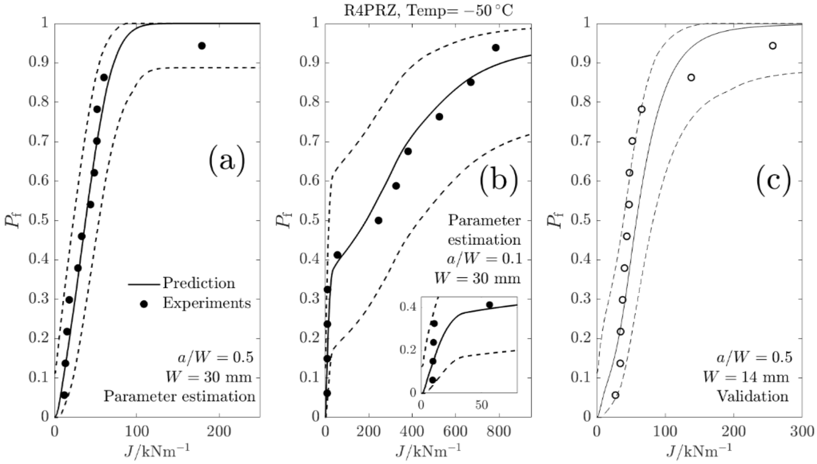

Figure 17. Comparison of the predicted failure probability with rank probabilities for the fracture tests (circles) of the reference material R4PRZ data set tested at a temperature -50 ˚C. (a) subset where $a/W = 0.5$ and $W = 30$ mm, (b) subset where $a/W = 0.1$ and $W = 30$ mm, and (c) subset where $a/W = 0.5$ and $W = 14$ mm. Subsets (a) and (b) were used for parameter estimation, subset (c) was used as validation of model predictions. Note, in (b) figure inset shows steep initial region of model prediction.

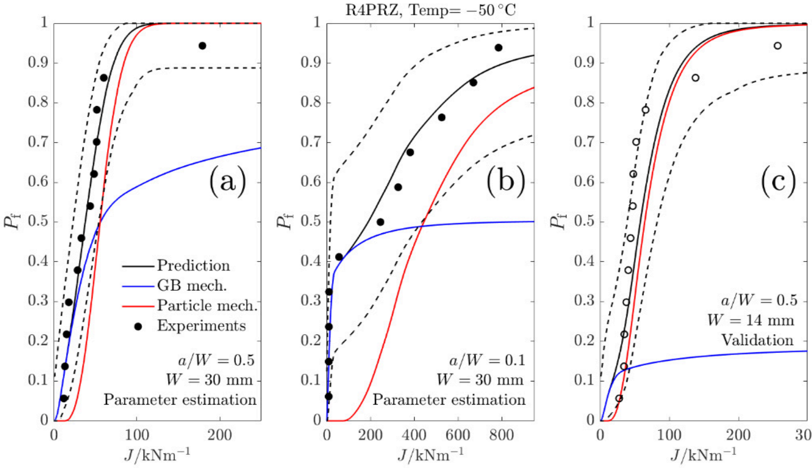

Figure 18. Comparison of the predicted failure probability with rank probabilities for the fracture tests (circles) of the reference material R4PRZ data set tested at a temperature -50 ˚C. Shown here are also the individual mechanisms calculated as if being single mechanism predictions. Note that the individual mechanisms as illustrated here do not sum up to the actual multi mechanism prediction since they are computed as single mechanism predictions and are for illustration purposes only.

6. Future work

The culmination of the work in this thesis is the multiple mechanism weakest link model. The model in itself contains some previously verified and some brand new elements. As presented, the model appears to work on the current data set at hand, however, further model development in tandem with experimental investigations is deemed necessary to further reinforce confidence in the model. Experiments where the fracture mechanisms could be separated more clearly would be a good starting point. This would enable improved understanding of the micro mechanism of failure, which could then be used to reshape or verify the basis of the model assumptions.

The temperature dependence of the mechanisms of brittle fracture initiation and their interactions is something that has been left out in the studies of this thesis. If experiments where the fracture mechanisms could be isolated could be devised, it would also be of great interest to study the temperature dependence of the two mechanisms.

Research on the interplay between ageing and ductile fracture mechanisms is also judged to be an area where future efforts could be placed.

Bibliography

[1] B. K. Sovacool, R. Andersen, S. Sorensen, K. Sorensen, V. Tienda, A. Vainorius, O. Marc Schirach och F. Bjørn-Thygesen, ”Balancing safety with sustainability: assessing the risk of accidents for modern low-carbon energy systems,” *Journal of Cleaner Production,* vol. 112, pp. 3952-3965, 2016.

[2] P. A. Kharecha och J. E. Hansen, ”Prevented Mortality and Greenhouse Gas Emissions from Historical and Projected Nuclear Power,” *Environmental Science and Technology,* vol. 47, nr 9, pp. 4889-4895, 2013.

[3] Statistiska Centralbyrån SCB, ”scb.se,” SCB, 30 November 2018. [Online]. Available: https://www.scb.se/hitta-statistik/sverige-i-siffror/miljo/elektricitet-i-sverige/. [Använd 27 May 2020].

[4] P. Bowen, S. G. Druce och J. F. Knott, ”Micromechanical modelling of fracture toughness,” *Acta Metallurgica,* vol. 35, nr 7, pp. 1735-1746, 1987.

[5] P. Bowen , S. G. Druce och J. F. Knott, ”Effects of microstructure on cleavage fracture in pressure vessel steel,” *Acta Metallurgica,* vol. 34, nr 6, pp. 1121-1131, 1986.

[6] Y. Qiao och A. Argon, ”Cleavage crack-growth resistance of grain boundaries in polycrystalline Fe-2%Si alloy: experiments and modeling,” *Mechanics of Materials,* vol. 35, pp. 129-154, 2003.

[7] Y. Qiao och A. Argon, ”Cleavage cracking resistance of high angle grain boundaries in FE-3%Si alloy,” *Mechanics of Materials,* vol. 35, pp. 313-331, 2003.

[8] A. Lambert-Perlade, A. Gourgues, J. Besson, T. Sturel och A. Pineau, ”An enhanced probabilistic model for cleavage fracture assessment accounting for local constraint effects,” *Metallurgical and Materials Transactions A,* vol. 35A, pp. 1039-1053, 2004.

[9] R. O. Ritchie, J. F. Knott och J. R. Rice, ”On the relationship between critical tensile stress and fracture toughness in mild steel,” *Journal of the Mechanics and Physics of Solids,* vol. 21, pp. 395-410, 1973.

[10] M. Kroon och J. Faleskog, ”A probabilistic model for cleavage fracture with a length scale - influence of material parameters and constraint,” *International Journal of Fracture,* vol. 118, pp. 99-118, 2002.

[11] ASTM International, ”E1921-15 Standard Test Method for Determination of Reference Temperature T0 for Ferritic steels in the Transition Range,” ASTM International, West Conshohocken, 2016.

[12] M. K. Miller, K. A. Powers, R. K. Nanstad och P. Efsing, ”Atom probe tomography characterizations of high nickel, low copper surveillance RPV welds irradiated to high fluences,” *Journal of Nuclear Materials,* vol. 437, pp. 107-115, 2013.

[13] K. Lindgren, M. Boåsen , K. Stiller, P. Efsing och M. Thuvander, ”Evolution of precipitation in reactor pressure vessel steel welds under neutron irradiation,” *Journal of Nuclear Materials,* vol. 488, pp. 222-230, 2017.

[14] K. Lindgren, ”Effects of Irradiation and Thermal Ageing on the Nanoscale Chemistry of Steel Welds,” Chalmers University of Technology, Gothenburg, 2018.

[15] D. Terentyev, X. He, G. Bonny, A. Bakaev, E. Shurkin och L. Malerba, ”Hardening due to dislocation loop damage in RPV model alloys: Role of Mn segregation,” *Journal of Nuclear Materials,* vol. 457, pp. 173-181, 2015.

[16] F. Bergner, F. Gillemot, M. Hernández-Mayoral, M. Serrano, G. Török, A. Ulbricht och E. Altstadt, ”Contributions of Cu-rich clusters, dislocation loops and nanovoids to the irradiation-induced hardening of Cu-bearing low-Ni reactor pressure vessel sttels,” *Journal of Nuclear Materials,* vol. 461, pp. 37-44, 2015.

[17] K. Lindgren, M. Boåsen, K. Stiller, P. Efsing och M. Thuvander, ”Cluster formation in in-service thermally aged pressurizer welds,” *Journal of Nuclear Materials,* vol. 504, pp. 23-28, 2018.

[18] L. Messina, M. Nastar, T. Garnier, C. Domain och P. Olsson, ”Exact ab initio transport coefficients in bcc FE-X (X = CR, Cu, Mn, Ni, P, Si) dilute alloys,” *Physical Review B,* vol. 90, p. 104203, 2014.

[19] L. Messina, M. Nastar, N. Sandberg och P. Olsson, ”Systematic electronic-structure investigation of substitutional impurity diffusion and flux coupling in bcc iron,” *Physical Review B,* vol. 32, p. 184302, 2016.

[20] K. Farrel, T. S. Byun och N. Hashimoto, ”Deformation mode maps for tensile deformation of neutron-irradiated structural alloys,” *Journal of Nuclear Materials,* vol. 335, pp. 471-486, 2004.

[21] A. H. Cottrell och R. J. Stokes, ”Effects of Temperature on the Plastic Properties of Aluminium Crystals,” *Proceedings of the Royal Society of London. Series A, Mathematical and Physical Sciences,* vol. 233, pp. 17-34, 1955.

[22] A. Luft, ”Microstructural processes of plastic instabilities in strengthened metals,” *Progress in Materials Science,* vol. 35, pp. 97-204, 1991.

[23] M. A. Sokolov, R. K. Nanstad och M. K. Miller, ”Fracture Toughness and Atom Probe Characterization of a Highly Embrittled RPV weld,” *Journal of ASTM International,* vol. 1, pp. 123-137, 2004.

[24] C. L. Briant och S. K. Banerji, ”Intergranular failure in steel: the role of grain boundary composition,” *International Metal Reviews,* pp. 164-199, 1978.

[25] C. J. McMahon, ”Intergranular Fracture in Steels,” *Materials Science and Engineering,* vol. 25, pp. 233-239, 1976.

[26] Y. I. Shtrombakh, B. A. Gurovich, E. A. Kuleshova, D. A. Maltsev, S. V. Fedotova och A. A. Chernobaeva, ”Thermal ageing mechanisms of VVER-1000 reactor pressure vessel steels,” *Journal of Nuclear Materials,* vol. 452, pp. 348-358, 2014.

[27] P. Gudmundson, ”A unified treatment of strain gradient plasticity,” *Journal of the Mechanics and Physics of Solids,* vol. 52, pp. 1379-1406, 2004.

[28] D. L. Holt, ”Dislocation cell formation in metals,” *Journal of Applied Physics,* vol. 41, pp. 3197-3201, 1970.

[29] M. F. Asbby, ”Deformation of plastically non-homogeneous materials,” *Philisophical Magazine,* vol. 21, pp. 399-424, 1970.

[30] B. Devincre, T. Hoc och L. Kubin, ”Dislocation mean free paths and strain hardening of crystals,” *Science,* vol. 320, pp. 1745-1748, 2008.

[31] Intergovernmental Panel on Climate Change (IPCC), ”Global Warming of 1.5 ˚C,” IPCC, Geneva, 2018.

[32] C. F. O. Dahlberg och J. Faleskog , ”Strain gradient plasticity analysis of the influence of grain size and distribution on the yield strength in polycrystals,” *European Journal of Mechanics A/Solids,* vol. 44, pp. 1-16, 2014.

[33] H. Nakata, K. Fuji, K. Fukuya, R. Kasada och A. Kimura, ”Grain Boundary Phosphorus Segregation in Thermally Aged Low Alloy Steelsw,” *Journal of Nuclear Science and Technology,* vol. 43, nr 7, pp. 785-793, 2006.

[34] A. Andrieu, A. Pineau, P. Joly, F. Roch och D. Ryckelynck, ”Influence of P and C intergranular segregation during manufacturing and ageing on the fracture toughness of nuclear pressure vessel steels,” *Procedia Materials Science,* vol. 3, pp. 655-660, 2014.

[35] E. D. Hondros och M. P. Seah, ”The Theory of Grain Boundary Segregation in Terms of Surface Adsorption Analogues,” *Metallurgical Transactions A,* vol. 8A, pp. 1363-13771, 1977.

[36] A. Pineau, A. Benzerga och T. Pardoen, ”Failure of metals I: Brittle and ductile failure,” *Acta Materialia,* vol. 104, pp. 424-483, 2016.

Summary of appended papers

Paper I: Evolution of the length scale in strain gradient plasticity

In this paper we assume a microstructural interpretation of the length scale in strain gradient plasticity theory. The length scale is assumed to relate to the dislocation spacing and the changes it undergoes during plastic deformation. From a relation between the dislocation cell size and the dislocation density an evolution law for the constitutive length scale as function of dislocation density has been derived. From this, several different evolution laws based on the available plastic strain field variables were derived and implemented in a 2D plane strain finite element code. This has been used to solve a test problem of pure bending, where the effects of the length scale evolution have been explored. Key results are that the strengthening effect of strain gradient plasticity is unaffected but that a decreased hardening is obtained and that in cases of strong evolution, a yield point drop phenomenon results.

Paper II: A generalized probabilistic model for cleavage fracture with a length scale - Influence of stress state and application to surface cracked experiments

In this paper we use a non-local weakest link model to study the effects of the stress measure used to model failure by cleavage fracture. We develop an effective normal stress measure capable of describing a state of generalized normal stress between the mean stress and the maximum principal stress, with a continuous transition in between. The model is applied to two experimental datasets from literature, as well as experiments on surface cracked specimens containing a semi-elliptical crack. The model is shown to be well capable of handling different kinds of crack tip constraint when predicting the cumulative probability of failure by cleavage fracture.

Paper III: Analysis of thermal embrittlement of a low alloy steel weldment using fracture toughness and microstructural investigations

In this paper we have conducted fracture toughness tests with the primary objective of investigating the influence of thermal ageing on the constraint effect on fracture toughness. Testing has been conducted on an in-service thermally aged weld metal from a replaced pressurizer from the Ringhals nuclear power plant and compared with a reference material from the same power plant. Atom Probe Tomography has also been carried out to investigate the effects of ageing on the nanostructure of the material. A key result is that a second brittle fracture mode from grain boundaries is introduced due to ageing besides the typical initiation from second phase particles. This alters the fracture toughness distribution so that a bimodality appears. The intergranular fracture mode is associated with very brittle behavior and partly cancels out the constraint effect on the fracture toughness.

Paper IV: A weakest link model for multiple mechanism brittle fracture – Model development and application

In this paper we develop a weakest link framework capable of handling brittle failure from two mechanisms, intergranular and transgranular failure. The expression for the probability of failure is derived from an assumption of mutual exclusivity, i.e. the final failure must stem from a unique mechanism. The mechanism for transgranular failure is used from previous studies, while the intergranular mechanism is inferred from micro mechanical analysis of polycrystalline aggregates using crystal plasticity. The fracture modeling itself has been carried out using a porous plastic Gurson model in order to accurately resolve the mechanical fields of the growing crack prior to the final brittle fracture. The influence of the ductile process on the brittle failure probability is also included. Key results include the accurate prediction of the fracture toughness distribution using the micro mechanically informed weakest link model, and a significant size effect of the intergranular mechanism that may lead to non-conservatism of small specimens.